SCIENTIFIC REPORTS

OPEN

SUBJECT AREAS:
METAMATERIALS
NANOPHOTONICS AND PLASMONICS

Received
30 September 2014

Accepted
30 December 2014

Published
23 January 2015

Correspondence and requests for materials should be addressed to Y.-C.L. (lanyc@mail.ncku.edu.tw) or D.P.T. (dptsai@phys.ntu.edu.tw)

Achieving planar plasmonic subwavelength resolution using alternately arranged insulator-metal and insulator-insulator-metal composite structures

Bo Han Cheng[1], Kai Jiun Chang[2], Yung-Chiang Lan[2] & Din Ping Tsai[1,3]

[1]Research Center for Applied Sciences, Academia Sinica, Taipei 115, Taiwan, [2]Department of Photonics and Advanced Optoelectronic Technology Center, National Cheng Kung University, Taiwan 70101, Taiwan, [3]Department of Physics, National Taiwan University, Taipei 10617, Taiwan.

This work develops and analyzes a planar subwavelength device with the ability of one-dimensional resolution at visible frequencies that is based on alternately arranged insulator-metal (IM) and insulator-insulator-metal (IIM) composite structures. The mechanism for the proposed device to accomplish subwavelength resolution is elucidated by analyzing the dispersion relations of the IM-IIM composite structures. Electromagnetic simulations based on the finite element method (FEM) are performed to verify that the design of the device has subwavelength resolution. The ability of subwavelength resolution of the proposed device at various visible frequencies is achieved by slightly varying the constituent materials and geometric parameters. The proposed devices have potential applications in multi-functional material, real-time super-resolution imaging, and high-density photonic components.

The demand for high-density photonics components has recently increased significantly. Surface plasmon-polaritons (SPPs) have attracted much attention because they can be confined on a subwavelength scale, helping to meet the requirement of high density[1]. The practicability of plasmonic based components must be determined. Comparing to the totally three dimensional fabrications, a class of novel optical devices named metasurface with a reduced dimensionality can be used to control the propagation of light[2,3]. Such optical devices have great potential for use in fabricating the next-generation high-density photonics components for their ease of fabrication. Actually, the multilayer hyperbolic metamaterials (MHMs) that consist of a few pairs of Ag and dielectric layers with the thickness of 10 nm have been fabricated by using such as focused ion beam (FIB)[4], e-beam lithography system[5–7], and physical vapor deposition (PVD)[4–6] with high reliability and accuracy. The recent literature has proposed many planar photonics components. These include the optical vortex plate[8], broadband quarter-wave plate[9,10], plasmonics lens[11], optical antenna[12,13], graphene devices that use transformation optics[14], the gradient meta-surface[15], and subwavelength imaging components[16–18]. As well as a low-cost of manufacture, tunability is critical.

Super- and hyper-lenses have been extensively studied owing to their ability of achieving subwavelength resolution[19,20]. Very recently, the hybrid-superlens-hyperlens was developed and demonstrated to exhibit super-resolution[21–23]. This device consists of both planar and concave metal-dielectric metamaterials. It overcomes the disadvantages of traditional near-field scanning optical microscopy, including low throughput, poor compatibility with samples, and an inability to obtain a complete image in a single scan. However, the range of materials that can be used to break optical diffraction is severely limited, and their operating bands may not be changed arbitrarily. Additionally, since they are three-dimensional structures, they are difficult to be integrated with other ultrathin photonic components.

This work proposes a planar subwavelength-resolved system that is based on alternately arranged insulator-metal (IM) and insulator-insulator-metal (IIM) composite structures. The dispersion relations of the alternately staked IM-IIM composite structures are studied. The ability of subwavelength resolution of the proposed struc-

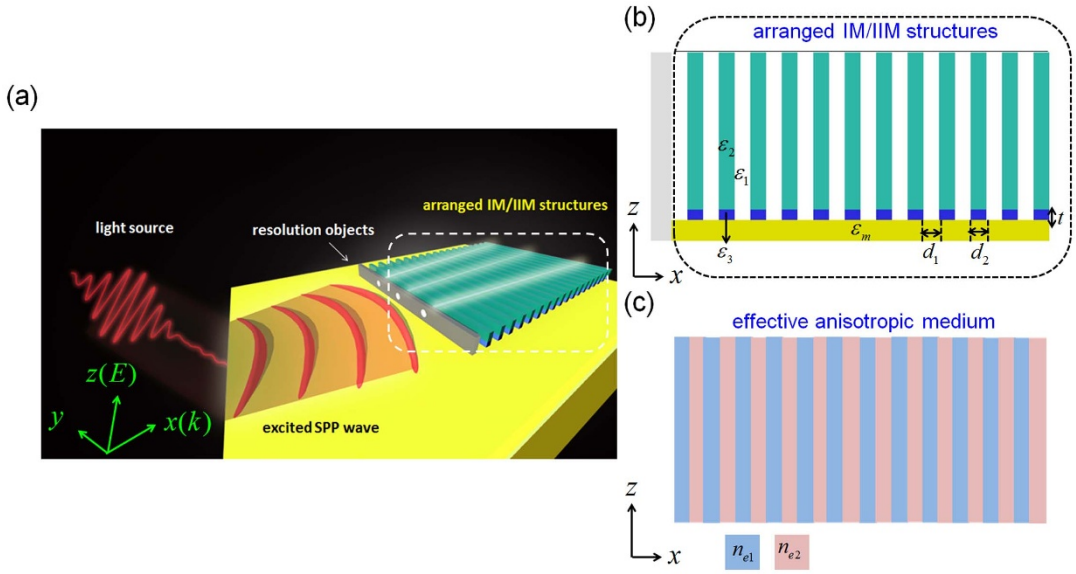

Figure 1 | Alternately arranged insulator-metal and insulator-insulator-metal composite structures. (a) Simulated structure. (b) Side-view of investigated system. (c) Structure equivalent to (b). Yellow region presents Cu or Ag with thickness of 50 nm.

tures is demonstrated by running electromagnetic simulations using the finite element method (FEM). This work develops the conceptual basis of a tunable flat photonics device that overcomes the optical diffraction limit. The proposed structure can be fabricated by using the same techniques for MHMs.

Results

Figure 1(a) presents the investigated structure, which consists of a few pairs of alternately arranged insulator-metal (IM) and insulator-insulator-metal (IIM) semi-infinite components with relative permittivities of $\varepsilon_1/\varepsilon_m$ and $\varepsilon_2/\varepsilon_3/\varepsilon_m$ respectively. In Fig. 1(a), d_1 and d_2 denotes the lengths of IM and IIM in the x direction, respectively, and t is the thickness of the middle insulator in IIM (ε_3). (The number of pairs is varied according to the operation conditions, as presented in Table 1.) Generally, SPPs in both IM and IIM structures are vertically confined (in the z-direction), but extended in the xy-plane. The effective refractive index of the IM or the IIM structure, n, is given by the formula, $n = c\cdot\mathrm{Re}[k]/\omega$, where k is the wavevector of the excited SPPs and can be determined by measuring the wavelength of the SPPs. (However, the sign of n is determined from the slope of the dispersion curve of the SPPs.) Therefore, the developed system (Fig. 1(a)) is viewed as an alternately stacked periodic system with an effective refractive index of n_{e1} (n_{e2}), as presented in Fig. 1(c).

The dispersion relation of the equivalent structure (Fig. 1(c)), which can be obtained using the transfer matrix method[24], is

$$\cos(k_\perp \Lambda) = \cos(k_{1\perp} d_1)\cos(k_{2\perp} d_2) - \frac{1}{2}\left(\frac{n_{e1}^2 k_{2\perp}}{n_{e2}^2 k_{1\perp}} + \frac{n_{e2}^2 k_{1\perp}}{n_{e1}^2 k_{2\perp}}\right)\sin(k_{1\perp} d_1)\sin(k_{2\perp} d_2), \quad (1)$$

where $k_{1\perp} = \sqrt{\left(\frac{n_{e1}\omega}{c}\right)^2 - k_{//}^2}$ and $k_{2\perp} = \sqrt{\left(\frac{n_{e2}\omega}{c}\right)^2 - k_{//}^2}$ are the x-directional component of wavevectors in the materials with effective refraction indices of n_{e1} and n_{e2}, respectively (and $k_{//}$ is the y- and z-directional wavevectors); $\Lambda = d_1 + d_2$ is the period of the alternately stacked system. Since $n = \sqrt{\varepsilon}\cdot\sqrt{\mu}$ (with $\mu = 1$), the long wave approximation ($\lambda >> \Lambda$, where λ is the wavelength of the incident source), and expansion of Eq. (1) to second order, the dispersion relation will be simplified to

$$\frac{k_{//}^2}{\varepsilon_\perp} + \frac{k_\perp^2}{\varepsilon_{//}} = k_0^2, \quad (2)$$

Table 1 | Material and geometric parameters of composite structure of alternately arranged IM–IIM that is used to obtained in Fig. 5.

Figure	5 (a)	5 (b)	5 (c)	5 (d)	5 (e)
Metal	Cu	Cu	Cu	Cu	Ag
Operating frequency (wavelength)	432.9 THz (682.52 nm)	431.63 THz (694.56 nm)	432.9 THz (682.52 nm)	350 THz (857 nm)	723.52 THz (414.35 nm)
Simulation domain X × Y × Z	440 × 800 × 130 (nm^3)	440 × 800 × 130 (nm^3)	440 × 800 × 130 (nm^3)	440 × 800 × 130 (nm^3)	440 × 550 × 120 (nm^3)
IM					
Width (d1)	15 nm	15 nm	15 nm	15 nm	15 nm
Height	130 nm	130 nm	130 nm	130 nm	120 nm
ε_1	2	2.25	2	2.25	4
IIM					
Width (d2)	15 nm	15 nm	× nm	15 nm	15 nm
Height (t)	8.0 nm	8.0 nm	× nm	8.0 nm	8.5 nm
ε_2	1	1	×	1	1
ε_3	4	4	×	4	6.5

where $\varepsilon_{\perp} = \left(\frac{d_1}{d_1+d_2}\frac{1}{\varepsilon_{e1}} + \frac{d_2}{d_1+d_2}\frac{1}{\varepsilon_{e2}}\right)^{-1}$ and $\varepsilon_{//} = \frac{\varepsilon_{e1}d_1 + \varepsilon_{e2}d_2}{d_1+d_2}$ are the effective relative permittivities in the perpendicular (x) and parallel (z) directions, respectively, and k_0 is the free space wave vector. (See Appendix A of supplementary information) Super-resolution applications that use the periodic layered system as shown in Fig. 1(c) require $\varepsilon_{\perp}\cdot\varepsilon_{//} < 0$ and $\varepsilon_{//} \to 0$[25]. Considering $\varepsilon_{e1}\cdot\varepsilon_{e2} < 0$, these criteria can be met. Therefore, an imaging device with the ability of one-dimensional subwavelength resolution can be realized by combining IM and IIM components.

Since the used components (IM or IIM) support SPPs at the dielectric-metal interface (as shown in the inset (i) in Figs. 2(a) and (b)), the structure in Fig. 1(a) can be regarded as a SPPs-based waveguide. First, the dispersion relations (frequency vs. wavevector, f – k diagrams) of IM and IIM are determined by simulation. Figures 2(a) and 2(b) present the simulated dispersion relations of the IM and IIM structures, respectively (The metal substrate is Cu, $\varepsilon_1 = 2$, $\varepsilon_2 = 1$, $\varepsilon_3 = 4$, and $t = 5$ nm.) Figure 2(a) reveals that the slopes (f/k_x) of the dispersion curve in all of wavevectors are positive. Hence, the IM structures have positive effective refractive indices. The wavelength of the excited SPPs falls as the operating frequency increase as shown in the inset in Fig. 2(a). Figure 2(b) indicates both positive and negative slopes of the dispersion relation in different wavevector regions. Between the two dashed lines in Fig. 2(b), one frequency corresponds to two wavevectors, indicating that two kinds of SPPs would be excited at this frequency. The excited SPPs with the larger (smaller) wavelength are associated with the lower-k (higher-k) mode. The lower-k (higher-k) mode has a positive (negative) slope, so the IIM structure has a positive (negative) refractive index in that mode. Notably, in the higher-k mode, the wavelength of the excited SPPs increases with the operating frequency (as shown in the insets in Fig. 2(b)). This relationship is a characteristic of a material with an effective negative refractive index[26,27].

The insets in Fig. 2(b) reveal that the propagation loss of the higher-k mode is very strong (meaning that this mode can only propagate a short distance.) The propagation loss declines as the operating frequency increases. For the higher-k mode, the relationship between the effective refractive index and the effective permittivity is $n = \sqrt{-\varepsilon_{eff}}$. The real and imaginary parts of the effective refractive index are determined by measuring the excited wavelength and propagation length of the higher-k mode, ($n = n_r + in_i$; here $n_i < n_r$) The corresponding relative permittivity is $\varepsilon_{eff} = -(n_r^2 - n_i^2 + i2n_rn_i) = \varepsilon_r + i\varepsilon_i$, (between the two dashed lines in Fig. 2(b)). (See Appendix B of supplementary information.) The effective refractive index and the relative permittivity of the IM structure (both of which are positive) are also determined from this measurement. Based on Figs. 2(a) and 2(b), the composite structure of alternatively arranged IM (with a positive relative permittivity) and IIM (with a negative relative permittivity) satisfies the requirement for subwavelength-resolved applications in particular frequency ranges.

To demonstrate further the tunability with subwavelength-resolved ability over whole visible region, the effects of changing the relevant parameters (such as: ε_m, ε_2, ε_3, and t) on the $f-k$ diagrams of IM and IIM are considered. Figure 3(a) displays the $f-k$ diagrams of the IM structure with Ag (blue line) and Cu (red line) metal substrates ($\varepsilon_1 = 2$). The $f-k$ diagrams approach different asymptotes (dashed lines) in Fig. 3(a). The asymptote frequency (the surface plasma frequency, ω_{sp}), is estimated using the formula, $\omega_{sp} = \omega_p/\sqrt{1+\varepsilon_1}$[28], and is proportional to the plasma frequency of the metal. Clearly, ω_{sp} decreases as ε_1 increases. Figure 3(b) shows the $f-k$ diagrams of IM structure for various values of ε_1 which verify the relation between ω_{sp} and ε_1 The yellow region in Fig. 3(b) is the range of frequencies at which the dispersion diagrams of IM and IIM intersect each other. The proposed subwavelength-resolved structure

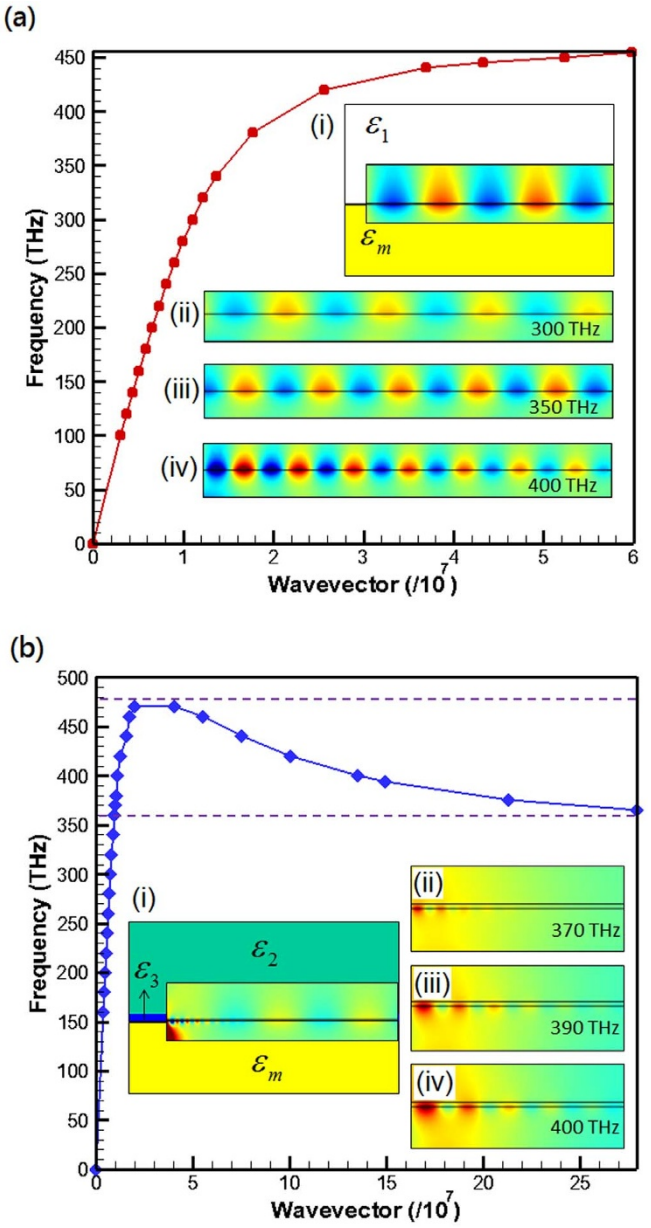

Figure 2 | $f-k$ diagrams. (a) IM (b) IIM structures. Insets (i) in (a) and (b): simulated structures and Hy field contours around insulator-metal interface (as shown in Fig. S2) Insets (ii) ~ (iv) in (a): magnetic field (Hy) contours at 300, 350 and 400 THz, respectively (in region where $f-k$ diagram has a positive slope). Insets (ii) ~ (iv) of (b): magnetic field (Hy) contours at 370, 390, and 400 THz, respectively (in region where $f-k$ diagram has both positive and negative slopes). Metal substrate is Cu. $\varepsilon_1 = 2$, $\varepsilon_2 = 1$, $\varepsilon_3 = 4$, and $t = 5$ nm.

operates in this region. Figures 3(a) and 3(b) also reveal that a metal with a larger ω_{sp} and a dielectric with a smaller ε_1 are required as the frequency of the incident light increases. Notably, to provide good resolution, the iso-frequency dispersion curve of the alternately arranged structure should have a hyperbolic form and the hyperbola must be as flat as possible (as shown in the inset in Fig. 3(b))[29].

Figure 3(c) presents the $f-k$ diagrams of the IIM structure for ε_3 layer with various values of t, a Cu metal substrate, $\varepsilon_2 = 1$ and $\varepsilon_3 = 4$ Figure 3(c) indicates that the $f-k$ diagrams in the higher-k mode in the negative slope region become flatter as t increases. The simulation results reveal that the feature of negative slope disappears once t increases to 28 nm (not shown here). This effect follows from the

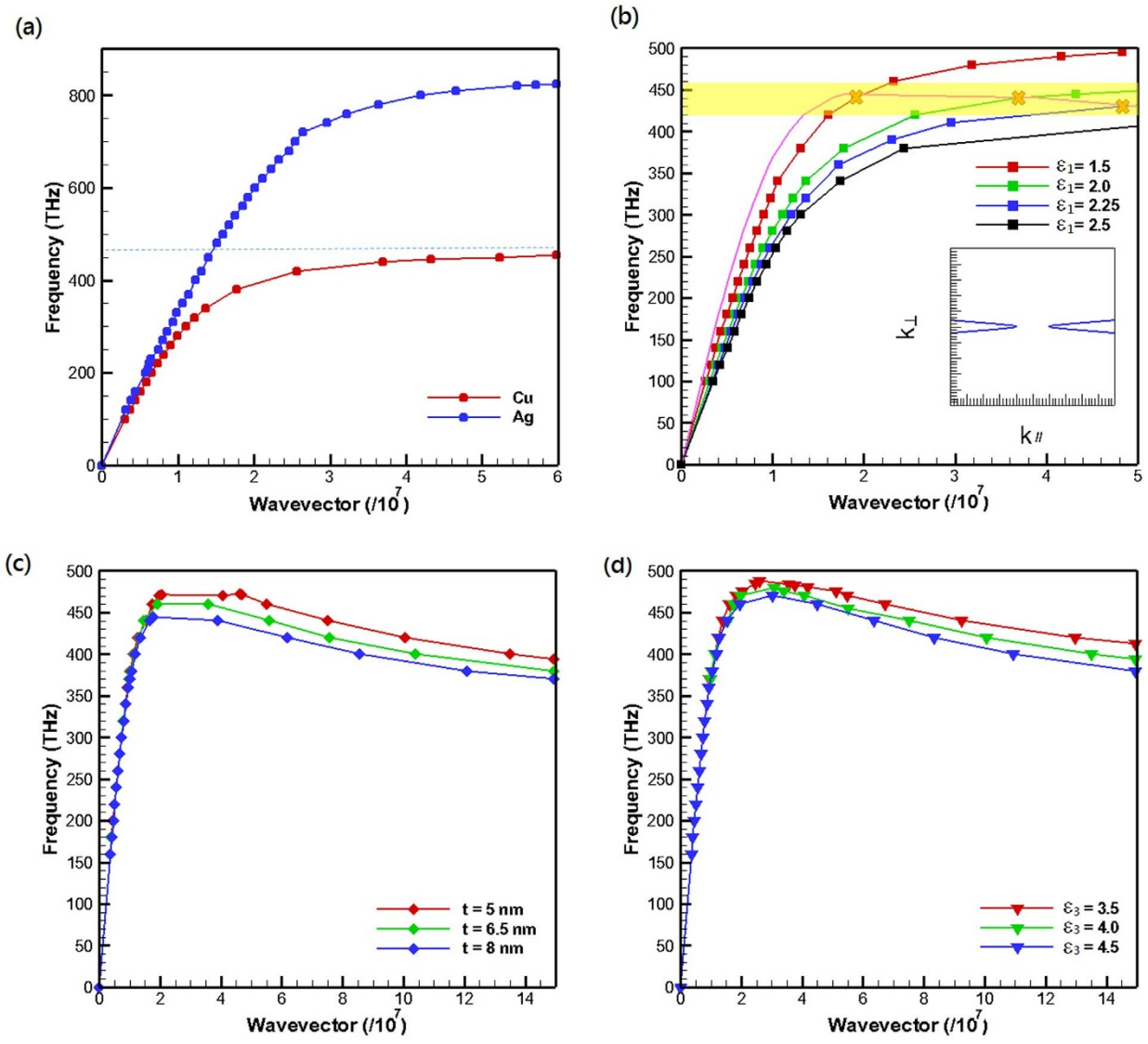

Figure 3 | (a)–(d): $f-k$ diagrams. (a) IM structure of Cu (red line) and Ag (blue line) metal substrate with$\varepsilon_1 = 2$ Dashed lines are asymptotes of ω_{sp} (b) IM structure for different values of ε_1 with Cu metal substrate. Purple line is dispersion diagram of IIM structure with Cu-substrate, $\varepsilon_2 = 1$, $\varepsilon_3 = 4$ and $t = 8$ nm. Inset: shows Hyperbolic iso-frequency curve (Eq. (2)) when alternately arranged IM-IIM structure fulfills the requirements for subwavelength resolution, which is that the point of intersection in yellow region. (c) IIM structure for different values of t with Cu metal substrate, $\varepsilon_2 = 1$, $\varepsilon_3 = 4$. (d) IIM structure for various values of ε_3 with Cu metal substrate, $\varepsilon_2 = 1$ and $t = 8$ nm.

gradual increase in the propagation losses of the higher-k (negative slope) mode[26] and implies that the thickness of the ε_3 layer provides a means of cutting off the negative slope of the higher-k mode. Figure 3(d) plots $f-k$ diagrams of the IIM structure for various ε_3 with the Cu metal substrate, $\varepsilon_2 = 1$ and $t = 8$ nm. Figure 3(d) shows that the frequency of the SPPs in the IIM structure in the negative slope region decreases as the value of ε_3 increases. Figure 3(d) indicates that the operating frequency of the IIM structure can be fine-tuned by varying the material parameter ε_3. In the following, this characteristic is exploited to modulate the operating frequency to meet the requirements for subwavelength resolution.

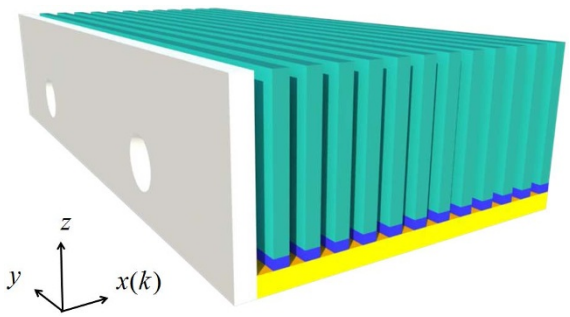

Figure 4 | **Schematic drawing of simulated structure.**

Next, the ability of subwavelength resolution of the proposed IM and IIM composite structure is demonstrated. Figure 4 plots the simulated structure. In Fig. 4, a chromium (Cr) mask with two holes is the object, which is in contact with the composite structure of alternately arranged IM and IIM. Two operating frequencies in the visible regime are considered – those of red light and violet light. The radius and the center-to-center distance of the two holes in red (violet) light are 35 nm and 320 nm (40 nm and 205 nm), respectively. Linearly polarized light (polarized in the x-z plane) is incident on the Cr mask. Owing to the super-resolution, the light that is diffracted from the tiny holes excites the SPPs and propagates through the proposed device. Finally, the subwavelength features are resolved at the end of the composite structure (Fig. 5).

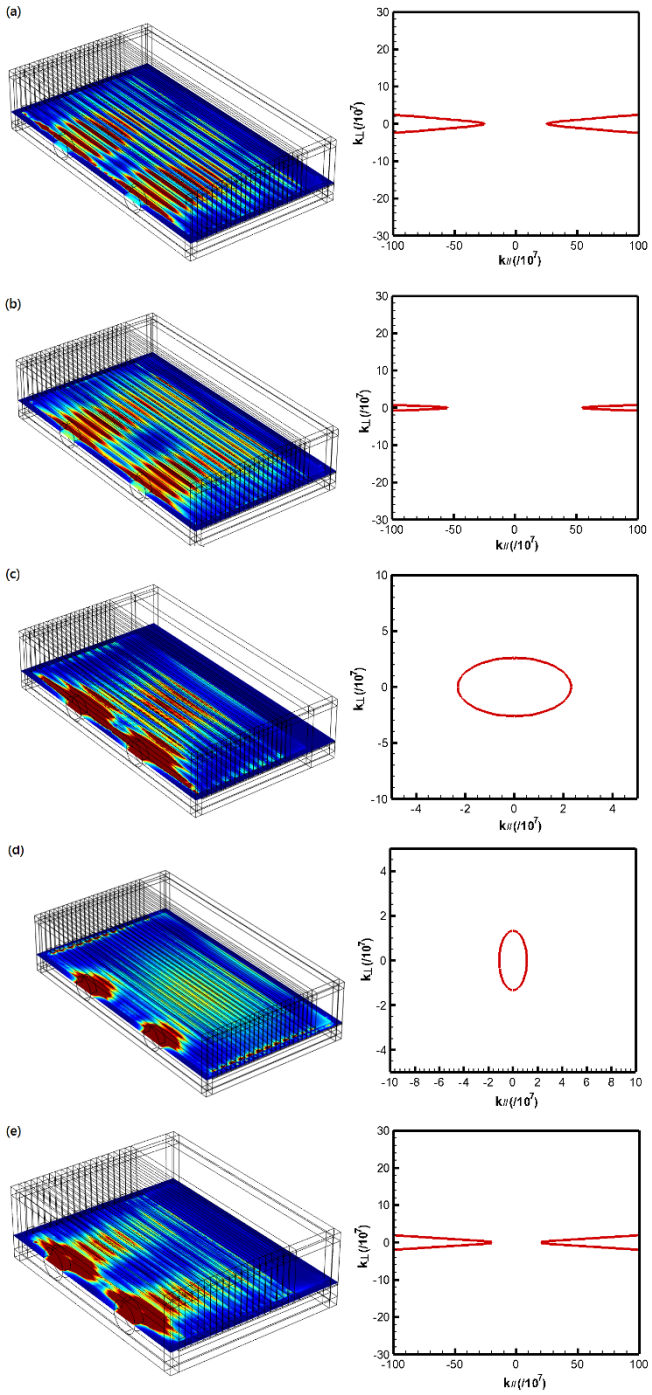

Figure 5 | Simulated time-averaged power flow contours and iso-frequency dispersion curves at various incident frequencies. (a) 432.9 THz (b) 413.63 THz, (c) 432.9 THz, (d) 350 THz, and (e) 723.52 THz. In (a), (b), (c) and (d), resolved objects have center-to-center distance of 320 nm. Radius of each hole is 35 nm. In (e), the center-to-center distance and radius are 205 and 40 nm, respectively. Mask is made of chromium with a thickness of 20 nm.

Figures 5(a) and 5(b) present the simulated time-averaged power flow contours and the corresponding iso-frequency dispersion curves for the structure in Fig. 4 at incident frequencies of 432.9 THz and 431.63 THz (red light), respectively. (Table 1 presents the material and geometric parameters of the IM and IIM structures.) For comparison, Fig. 5(c) plots the contours and iso-frequency dispersion curve at 432.9 THz for the imaging system that includes only the IM structure (i.e. the dielectric materials (ε_2 and ε_3) of the IIM structure are removed). These contours are extracted in the *x*-*y* plane and 2.5 nm above the top metal substrate. Figures 5(a) and 5(b) reveal that the two tiny holes are resolved at the end of the proposed system with the alternate components. The iso-frequency dispersion curves in these figures satisfy the requirements for sub-wavelength resolution, as they are hyperbolic. Conversely, Fig. 5(c) shows that, when only the IM structure is utilized, the light that is diffracted from one of the two tiny holes (in the form of SPPs) interferes with that from the other in the system. These holes cannot be resolved at the end of the system. The iso-frequency dispersion curve becomes elliptical. Figure 5(d) displays the time-averaged power flow contours and the iso-frequency dispersion curve obtained using the same structure as in Figs. 5(a) and (b) but with an incident frequency of 350 THz. Figure 5(d) shows that the diffraction occurs and the holes cannot be resolved at the end of the system because the requirements for subwavelength resolution are not met, as mentioned above (since the so-frequency dispersion curve is elliptical). Finally, Fig. 5(e) plots the simulated time-averaged power flow contours and the iso-frequency dispersion curve for the structure in Fig. 4 but with an incident frequency of 732.52 THz (violet light) and with various material and geometric parameters also given in Table 1. Figure 5(e) clearly reveals that the metal substrate and geometric parameters can be changed to resolve the two tiny holes with a center-to-center distance of less than half of the incident wavelength in the violet light region. It's also worth mentioning that, for above successfully resolved cases (Figs. 5(a), 5(b) and 5(e)), the two holes on the Cr mask still can be resolved when their z-directional positions are changed. It is originated from that the SPPs on the IM structure can be excited by the evanescent waves that emit from the objects and the above mentioned mechanism still work. As an example, considering two holes with centers locating at 30 nm and 80 nm, respectively, above the metal top (the other conditions are the same as Fig. 5(e)), our simulation results reveal that both holes can be resolved at the end of the proposed device. (See Appendix C of supplementary information) This feature enables the proposed structure to transform the two-dimensional objects into the one-dimensional image.

Table 1 further indicates that small changes in the material and geometric parameters change the frequency at which subwavelength resolution is obtained. For example, in Figs. 5(a) and 5(b), small changes in ε_1 (from 2 to 2.25) and t (from 8.5 nm to 8 nm) change the operating frequency of subwavelength resolution from 432.9 THz to 413.63 THz, revealing that more parameters of the proposed structure can be adjusted to achieve super-resolution function for a light source with various frequency. The fabrication tolerances of the designed geometric parameters d_1, d_2 and t are also examined. For d_1 and d_2, according to Ref. 5, the thickness error of sputtered film (10 nm Ag and 10 nm Si) for the MHMs is not larger than 1 nm. With this thickness error, Eq. (2) shows that the iso-frequency dispersion relation in Figs. 5(a), 5(b) and 5(e) still have the hyperbolic form. Hence, the objects (two holes) can still be resolved. That is to say, the error in thickness of the multilayers that is caused by the state-of-art technology has little effect on the designed parameters d_1 and d_2. Conversely, for the designed parameter $t = 8$ nm in Fig. 5(a), an error of 3 nm in t will cause a deviation of 22 THz (about 5%) from the operation frequency designed at 433 THz. (See Appendix D of supplementary information.) Based on these analyses, the proposed design is practical for the state-of-art technology.

Notably, the structure that is proposed herein is better than those developed elsewhere[21–23], in occupying less space, being easier to fabricate, and having a flexible design with super-resolution. Our investigations exhibit that, by designing the iso-frequency dispersion curve (i.e. $k_{//}$ *vs.* $k_{\perp}$, as shown in Fig. 5), the propagating waves in the IM-IIM composite structures can be manipulated. By suitably controlling the incident angles and positions of launched sources, the

planar subwavelength focusing of surface plasmon beam can be achieved by using the proposed structure[30]. Some other fantastic phenomena that are based on the SPPs wave, such as the feature of scattering-free[31], total-external-reflection[27], all-angle negative refractive[32], and spatial plasmonic Bloch oscillations[33], can also be implemented by using the proposed structure. Moreover, the typically resolvable size depends on the geometry and material parameters, and hence can be deigned. (For example, this size is about 200 nm for the incident frequency of 723.52 THz in the design of Fig. 5(e).) Therefore, the proposed planar structures have a wide range of potential applications in different fields (owing to their periodic construction) such as in hyperbolic materials[34,35], near-zero materials[36,37], and highly efficient nano-scale mirrors[27].

Discussion

A planar subwavelength-resolved device (at the visible frequencies) that is based on alternately arranged IM and IIM composite structures is proposed and analyzed. The IM and IIM components in the proposed device can be viewed as forming an effective optical medium with positive and negative refractive indices, respectively. The iso-frequency dispersion curves of the alternately arranged IM-IIM composite structures are hyperbolic form. The FEM electromagnetic simulations confirm that the device has a subwavelength resolution. The subwavelength resolution of the proposed device can be achieved at different visible frequencies by slightly changing the constituent materials and geometric parameters. More importantly, the constituent materials that satisfy the criteria for overcoming limits on optical diffraction are available in nature. The device that is developed herein has potential applications in real-time subwavelength imaging and high-density photonic components.

Methods

All simulations herein are conducted in the commercial electromagnetic software COMSOL Multiphysics, using the finite element method. The metals in Fig. 1(a) and Fig. 4 are copper (Cu) and silver (Ag). The Drude model applies as follows[28,38,39],

$$\varepsilon_{Cu}(\omega) = 1 - \frac{{\omega_{p1}}^2}{(\omega^2 + i\gamma_1\omega)} \tag{3}$$

$$\varepsilon_{Ag}(\omega) = 6 - \frac{{\omega_{p2}}^2}{(\omega^2 + i\gamma_2\omega)}, \tag{4}$$

where ω is the angular frequency; $\omega_{p1} = 5 \times 10^{15}$ *rad/s* and $\omega_{p2} = 1.5 \times 10^{16}$ *rad/s* are the bulk plasma frequencies of Cu and Ag, respectively, and $\gamma_1 = 5 \times 10^{13}$ *rad/s* ($\gamma_2 = 7.73 \times 10^{13}$ *rad/s*) is the damping constant of Cu (Ag). Here, the material with dielectric constant ε_1 (ε_2 and ε_3) in Fig. 5(a) and 5(b) is SiO_2 (Air and HfO_2)[40]. And the material with dielectric constant ε_1 (ε_2 and ε_3) for operating in higher frequency (Fig. 5(e)) is Y_2O_3 (Air and Nb2O5)[40]. To suppress the noise reflected from the simulated boundaries, perfectly matched layers are used outside the structure. To excite the SPPs of interest, a linearly polarized plane source whose electric field oscillates in the *xz*-plane is launched at $x = 0$ (as in the end-fire method)[41,42], producing the non-radiation mode SPPs on the IM (IIM) interface[26].

1. Barnes, W. L., Dereux, A. & Ebbesen, T. W. Surface plasmon subwavelength optics. *Nature* **424**, 824–830 (2003).
2. Kildishev, A. V., Boltasseva, A. & Shalaev, V. M. Planar photonics with metasurfaces. *Science* **339**, 1232009 (2013).
3. Zhang, J., Xiao, S., Wubs, M. & Mortensen, N. A. Surface plasmon wave adapter designed with transformation optics. *ACS Nano* **5**, 4359–4364 (2011).
4. Poddubny, A., Iorsh, I., Belov, P. & Kivshar, Y. Hyperbolic metamaterials. *Nat. Photon.* **7**, 948–957 (2013).
5. Lu, D., Kan, J. J., Fullerton, E. E. & Liu, Z. Enhancing spontaneous emission rates of molecules using nanopatterned multilayer hyperbolic metamaterials. *Nature Nanotech.* **9**, 48–53 (2014).
6. Yang, X., Yao, J., Rho, J., Yin, X. & Zhang, X. Experimental realization of three-dimensional indefinite cavities at the nanoscale with anomalous scaling laws. *Nat. Photon.* **6**, 450–454 (2012).
7. Yang, J. K. W. & Berggren, K. K. Using high-contrast salty development of hydrogen silsesquioxane for sub-10-nm half-pitch lithography. *J. Vac. Sci. Technol. B* **25**, 2025–2029 (2007).
8. Litchinitser, N. M. Applied Physics. Structured light meets structured matter. *Science* **37**, 1054–1055 (2012).
9. Yu, N. *et al.* Broadband background-free quarter-wave plate based on plasmonic metasurfaces. *Nano Lett.* **12**, 6328–6333 (2012).
10. Roberts, A. & Lin, L. Plasmonic quarter-wave plate. *Opt. Lett.* **37**, 1820–1822 (2012).
11. Liu, Y., Zentgraf, T., Bartal, G. & Zhang, X. Transformational plasmon optics. *Nano Lett.* **10**, 1991–1997 (2010).
12. Ni, X., Emani, N. K., Kildishev, A. V., Boltasseva, A. & Shalaev, V. M. Broadband light bending with plasmonic nanoantennas. *Science* **335**, 427 (2012).
13. Yu, N. *et al.* Flat photonics: Controlling wavefronts with optical antenna metasurfaces. *IEEE J. Sel. Top. Quantum Electro.* **19**, 4700423 (2013).
14. Vakil, A. & Engheta, N. Transformation optics using grapheme. *Science* **332**, 1291–1294 (2011).
15. Sun, S. L. *et al.* Gradient-index meta-surfaces as a bridge linking propagating waves and surface waves. *Nat. Mater.* **11**, 426–431 (2012).
16. Smolyaninov, I. I., Hung, Y.-J. & Davis, C. C. Magnifying superlens in the visible frequency range. *Science* **315**, 1699–1701 (2007).
17. Smolyaninov, I. Two-dimensional metamaterial optics. *Laser Phys. Lett.* **7**, 259–269 (2010).
18. Li, P. & Taubner, T. Broadband subwavelength imaging using a tunable graphene-lens. *ACS Nano* **6**, 10107–10114 (2012).
19. Bloemer, M. J., D'Aguanno, G., Scalora, M., Mattiucci, N. & Ceglia, D. de. Energy considerations for a superlens based on metal/dielectric multilayers. *Opt. Express* **16**, 19342–19353 (2008).
20. Lee, H., Liu, Z., Xiong, Y., Sun, C. & Zhang, X. Development of optical hyperlens for imaging below the diffraction limit. *Opt. Express* **15**, 15886–15891 (2007).
21. Cheng, B. H., Ho, Y. Z., Lan, Y. C. & Tsai, D. P. Optical hybrid-superlens-hyperlens for super resolution imaging. *IEEE J. Sel. Top. Quantum Electron.* **19**, 4601305 (2013).
22. Wang, Y. T. *et al.* Gain-assisted hybrid-superlens-hyperlens for nano imaging. *Opt. Express.* **20**, 22953–22960 (2012).
23. Cheng, B. H., Lan, Y. C. & Tsai, D. P. Breaking optical diffraction limitation using optical hybrid-superlens-hyperlens with radically polarized Light. *Opt. Express* **21**, 14898–14906 (2013).
24. Yariv, A. & Yeh, P. *Photonics: Optical Electronics in Modern Communications, 6th ed.* (Oxford University Press, Oxford, 2006).
25. Salandrino, A. & Engheta, N. Far-field subdiffraction optical microscopy using metamaterial crystals: theory and simulations. *Phys. Rev. B* **74**, 075103 (2006).
26. Dionne, J. A., Verhagen, E., Polman, A. & Atwater, H. A. Are negative index materials achievable with surface plasmon waveguides? A case study of three plasmonic geometries. *Opt. Express* **16**, 19001–19017 (2008).
27. Stockman, M. I. Slow propagation, anomalous absorption, and total external reflection of surface plasmon polaritons in nanolayer systems. *Nano Lett.* **6**, 2604–2608 (2006).
28. Karalis, A., Lidorikis, E., Ibanescu, M., Joannopoulos, J. D. & Soljacić, M. Surface-plasmon-assisted guiding of broadband slow and subwavelength light in air. *Phys. Rev. Lett.* **95**, 063901 (2005).
29. Wood, B., Pendry, J. B. & Tsai, D. P. Directed subwavelength imaging using a layered metal-dielectric system. *Phys. Rev. B* **74**, 115116 (2006).
30. Verslegers, L., Catrysse, P. B., Yu, Z. & Fan, S. Deep-subwavelength focusing and steerging of light in an aperiodic metallic waveguide array. *Phys. Rev. Lett.* **103**, 033902 (2009).
31. Elser, J. & Podolskiy, V. A. Scattering-free plasmonic optics with anisotropic metamaterials. *Phys. Rev. Lett.* **100**, 066402 (2008).
32. Fan, X., Wang, G. P., Lee, J. C. W. & Chan, C. T. All-angle broadband negative refraction of metal waveguide arrays in the visible range: theoretical analysis and numerical demonstation. *Phys. Rev. Lett.* **97**, 073901 (2006).
33. Lin, W., Zhou, X. & Wang, G. P. Spatial Bloch oscillations of plasmons in nanoscale metal waveguide arrays. *Appl. Phys. Lett.* **91**, 243113 (2007).
34. Zhukovsky, S. V., Kidwai, O. & Sipe, J. E. Physical nature of volume plasmonpolaritons in hyperbolic metamaterials. *Opt. Express* **21**, 14982–14987 (2013).
35. Guo, Y. & Jacob, Z. Thermal hyperbolic metamaterials. *Opt. Express* **21**, 15014–15019 (2013).
36. Engheta, N. Pursuing Near-Zero Response. *Science* **340**, 286 (2013).
37. Ourir, A., Maurel, A. & Pagneux, V. Tunneling of electromagnetic energy in multiple connected leads using near-zero materials. *Opt. Lett.* **38**, 2092–2094 (2013).
38. Johnson, P. B. & Christy, R. W. Optical constants of the noble metals. *Phys. Rev. B* **74**, 4370–4379 (1972).
39. Kittel, C. *Introduction to Solid State Physics, 7th ed.* (John Wiley & Sons, New York, 1996).
40. Polyanskiy, M. *RefractiveIndex,INFO.* (2008) Available at: http://refractiveindex.info. (Date of access: 6th December 2014).
41. Stegeman, G. I., Wallis, R. F. & Maradudin, A. A. Excitation of surface polaritons by end-fire coupling. *Opt. Lett.* **8**, 386–388 (1983).
42. Leosson, K., Nikolajsen, T., Boltasseva, A. & Bozhevolnyi, S. I. Long-range surface plasmonpolariton nanowire waveguides for device applications. *Opt. Express* **14**, 314–319 (2006).

Acknowledgments

The authors acknowledge financial support from Ministry of Science and Technology, Taiwan (Grant Nos. 101-2112-M-006-002-MY3, 103-2745-M-002-004-ASP,

102-2911-I-002-505 and 103-2911-I-002-594) and Academia Sinica (Grant No.AS-103-TP-A06). They are also grateful to National Center for Theoretical Sciences, Taipei Office, Molecular Imaging Center of National Taiwan University, National Center for High-Performance Computing, Taiwan, and Research Center for Applied Sciences, Academia Sinica, Taiwan for their support.

Author contributions

B.H.C. and K.J.C. jointly conceived the idea. B.H.C. and K.J.C. designed and performed the calculations. Y.C.L. and D.P.T. assisted in the analyzing and discussion of the results. B.H.C., Y.C.L. and D.P.T. prepared the manuscript. Y.C.L. and D.P.T. supervised and coordinated all the work. All authors commented on the manuscript.

Additional information

Supplementary information accompanies this paper at http://www.nature.com/scientificreports

Competing financial interests: The authors declare no competing financial interests.

How to cite this article: Cheng, B.H., Chang, K.J., Lan, Y.-C. & Tsai, D.P. Achieving planar plasmonic subwavelength resolution using alternately arranged insulator-metal and insulator-insulator-metal composite structures. *Sci. Rep.* **5**, 7996; DOI:10.1038/srep07996 (2015).